VI ECCOMAS Thematic Conference on the Mechanical Response of Composites
COMPOSITES 2017
J.J.C. Remmers and A. Turon (Editors)

MULTISCALE FIBER KINKING: COMPUTATIONAL MICROMECHANICS AND A MESOSCALE CONTINUUM DAMAGE MECHANICS MODELS

Miguel Herráez[*,1,2] , Andrew C. Bergan[3], Carlos González[1,2], Claudio S. Lopes[2]

[1]Department of Materials Science, Polytechnic University of Madrid,
E.T.S. de Ingenieros de Caminos, 28040 Madrid, Spain

[2]IMDEA Materials
C/Eric Kandel 2, 28906 Getafe, Madrid, Spain
miguel.herraez@imdea.org
carlosdaniel.gonzalez@imdea.org
claudiosaul.lopes@imdea.org

[3]NASA Langley Research Center, Structural Mechanics and Concepts Branch
Hampton, Virginia 23681, U.S.A.

Key words: Fiber kinking, Computational micromechanics, Multiscale

Summary: *In this work, the fiber kinking phenomenon, which is known as the failure mechanism that takes place when a fiber reinforced polymer is loaded under longitudinal compression, is studied. A computational micromechanics model is employed to interrogate the assumptions of a recently developed mesoscale continuum damage mechanics (CDM) model for fiber kinking based on the deformation gradient decomposition (DGD) and the LaRC04 failure criteria.*

1 INTRODUCTION

There is a need for more accurate mesoscale models for predicting the fiber kinking failure mode in fiber reinforced polymer (FRP) laminates for use in progressive damage analysis (PDA) codes. One factor limiting the accuracy of predictions by many state-of-the-art PDA codes when fiber kinking is active is that most of the physical characteristics of the fiber kinking process are ignored. The conventional continuum damage mechanics (CDM) approach uses the same phenomenological model used commonly for longitudinal tension for longitudinal compression also [1, 2]. The constitutive law typically follows a linear or bilinear softening up to the material point is fully damaged and a stress-free state is reached. Such a model is not reasonable for compression failure modes in FRP laminates since it is not expected that stress will reduce to zero. Instead, it is intuitive that as long as the material remains in contact with itself, some residual stress state will exist as damage evolves.

The fiber kinking theory introduced by Budiansky offers a physically based approach to kinkband initiation and propagation [3, 4]. Kinking theory identifies the relevant mechanisms in kinkband formation as a combination of an initial fiber misalignment, shear stress-strain behavior that is nonlinear, and large fiber rotation. Fiber kinking theory produces the

characteristic mechanical response shown in Figure 1a where, once the compressive strength X_c, is reached, the stress drops unstably to a plateau crush stress level. The kink band is idealized as shown in Figure 1b with a fiber misalignment angle, φ, band angle, β, and band width, w_{kb}. If the shear nonlinearity follows a Ramberg-Osgood behavior, $\gamma = (\tau + \alpha\tau^{\eta})/G$, Budiansky's theory predicts the strength as,

$$X_c = \frac{G_{12}}{1 + \eta\,\alpha^{1/\eta}\left(\frac{G_{12}\,\varphi_0}{\eta - 1}\right)^{\frac{\eta-1}{\eta}}} \tag{1}$$

where, G_{12}, is the in-plane shear modulus, α and η define the nonlinear shear stress-strain curve, and φ_0 is the initial fiber misalignment. It is important to notice that this closed-form solution assumes $\beta = 0°$.

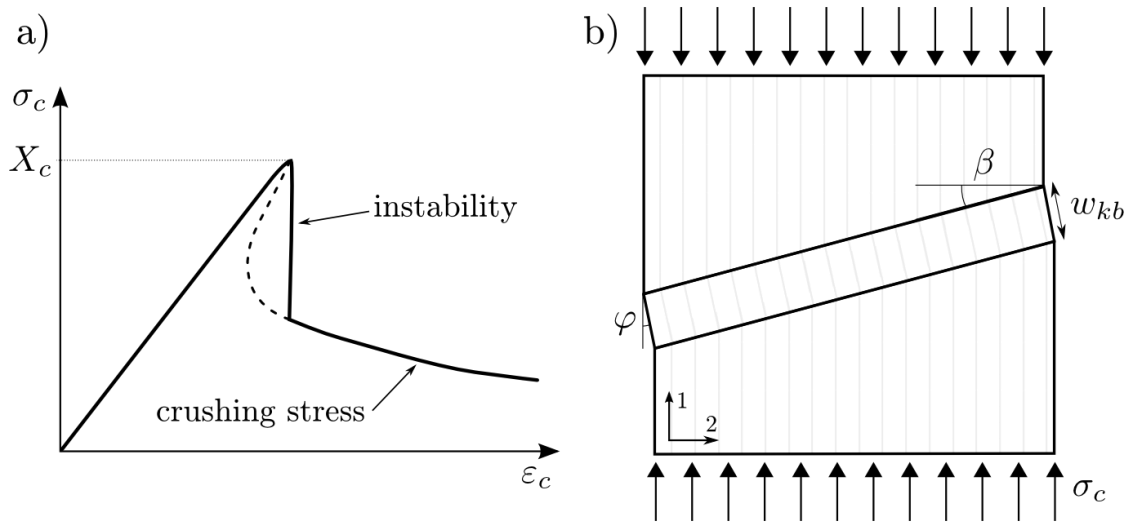

Figure 1. The characteristic constitutive response predicted by fiber kinking (a) and the idealization of the kink band formation (b)

Validation of models for fiber kinking is a challenging undertaking due to the instability of the process. Most experimental configurations exhibit unstable failure or interaction of kinking with other damage mechanisms yielding limited data or challenging cases for model validation. In the absence of detailed experimental investigations, computational micromechanics has much utility in providing an alternative basis for evaluating assumptions of models derived at the mesoscale. Recently, high-fidelity three-dimensional (3-D) computational micromechanical models of fiber kinking have been introduced [5, 6] and have shown promising as sources of insights into the fiber kinking process.

In this paper, a computational micromechanical model for fiber kinking is interrogated to evaluate the assumptions of a mesoscale model proposed and further developed by Bergan and Leone [7]. Some of the details of this constitutive model are discussed in Section 2. In the following section, the computational micromechanical model developed by Naya et al. [5] is

adapted for use in evaluating the assumptions of the mesoscale model. Finally, in Section 4 a direct comparison between the two models is presented.

2 MESOSCALE CONSTITUTIVE MODEL

The mesoscale constitutive model represents the fiber kinking phenomenon considering geometric and shear nonlinearities. The model includes the kinematics of the fiber kinking process by tracking fiber misalignment, φ, throughout loading. The characteristic mechanical response shown in Figure 1a is not prescribed in the model, but is a result of the shear nonlinearity and the fiber rotation. No longitudinal compression fracture energy needs to be specified. The details of the implementation are presented in detail in [7, 8].

The initial misalignment angle, φ_0, accounts for fiber misalignments and other manufacturing defects that contribute to fiber kinking initiation. Rearranging Eq. (1), the initial fiber misalignment is,

$$\varphi_0 = \frac{\eta - 1}{G_{12}} \left(\frac{G_{12} - X_C}{X_C \, \eta \, \alpha^{1/\eta}} \right)^{\frac{\eta}{\eta - 1}} \tag{2}$$

Material models that exhibit strain-softening behavior are susceptible to mesh sensitivity when strain localizes. In conventional CDM models, this deficiency is often addressed with Bažant's crack band theory [9] in which the energy dissipated is scaled by the element size. In the present model, there is no crack surface on which traction goes to zero and therefore the crack band theory is not applicable. Nonetheless, there is an inherent mesh sensitivity since the model includes a strain-softening response leading to strain localization in a band of elements after the strength is reached. The method used herein is analogous to the strain decomposition method by Costa et al. [10] and follows previous work by Bergan and Leone [7]. The model has been implemented in Abaqus/Explicit [15] as a user material subroutine (VUMAT).

The kink band width, w_{kb}, is assumed to be smaller than the element size such that the element can be decomposed into an undamaged material region and a kink band region, as shown in Figure 2. In the kink band region, shear nonlinearity is enabled, whereas in the undamaged material region the shear response is linear. The deformation gradient decomposition (DGD) approach [7, 8] is used to enforce continuity and equilibrium between the undamaged and kink band regions. The DGD approach is enabled (and thus the element is decomposed) when plastic strain becomes non-negligible. However, kink band width, w_{kb}, cannot be predicted by the model and it is required as an input. Values reported in the literature range from 50 μm to 200 μm from experimental observations [11–14] and numerical models [5, 6].

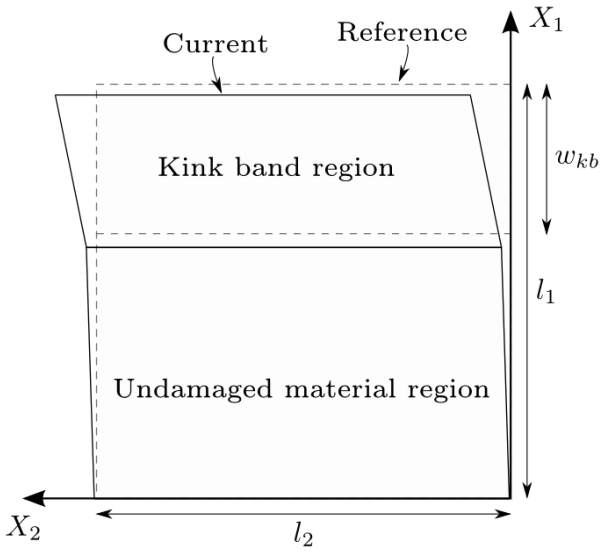

Figure 2. Schematic representation of the model: decomposition into the kink band and the undamaged region

3 COMPUTATIONAL MICROMECHANICS MODEL

In this section, the micromechanical finite element model (FEM) is described including the geometry, discretization, and material properties. Subsequently, a calibration study that was conducted to demonstrate equivalence between the shear behavior of the mesoscale and micromechanical model is described.

A 3-D single-fiber micromechanical model is used to interrogate assumptions of the mesoscale model. The micromechanical FEM is an extension of the single-fiber model described in Naya et al. [5] where it was demonstrated that a single-fiber representative volume element (RVE) produces strength predictions in good agreement with a multi-fiber RVE. The 3-D single-fiber model is used here since the model is a good compromise between computational expense and accuracy. A trade-study between several modeling strategies concluded that a single-fiber and multi-fiber two dimensional models were less accurate than 3-D single fiber models. Multi-fiber 3-D models were discarded due to convergence difficulties and computational expense.

3.1 Single-fiber 3-D model for fiber kinking

The model represents a single carbon fiber extruded in the longitudinal z-direction along the half wavelength of a sinusoidal curve of length, L, as shown in Figure 3. The initial misalignment is geometrically introduced according to,

$$y(z) = L\frac{\varphi_0}{\pi}\left(1 - \cos\left(\pi\frac{z}{L}\right)\right) \tag{3}$$

$$y'(z) = \varphi_0 \sin\left(\pi\frac{z}{L}\right) \tag{4}$$

such that the initial misalignment varies along the length of the fiber with the material orientation given by Eq. 4, see Figure 3d.

The fiber diameter is 7.09 μm and the fiber volume fraction is 65%. The model is discretized using 8-node fully integrated isoparametric elements (C3D8). The in-plane mesh size is around 1 μm, while in the longitudinal direction it is 10 μm, and the model length is set to 500 μm. Periodicity of the mechanical fields is guaranteed by the application of periodic boundary conditions (PBC). Gutkin et al. [16] showed that PBC can be applied on single-fiber models for longitudinal compressive strength prediction, X_C, at the expense of inducing $\beta = 0°$. Simulations were conducted in Abaqus/Standard under a dynamic implicit scheme.

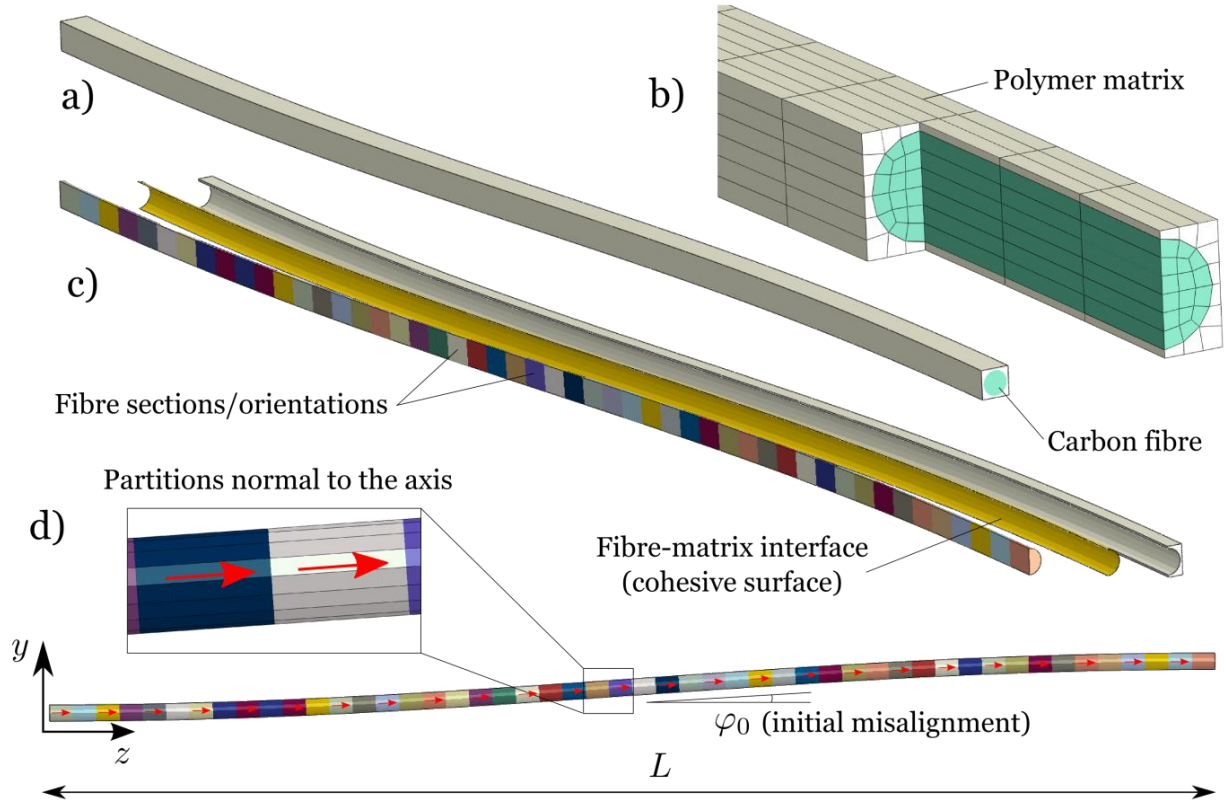

Figure 3. Illustration of the single-fiber 3-D model (a), detail of the mesh (b), exploded cut view of the model (c), and side view with detail of the longitudinal mesh and material orientation (d)

The material system used in this study is AS4/8552 carbon epoxy. Carbon fibers are assumed to behave as linear elastic transversely isotropic solids with the elastic constants shown in Table 1. The matrix behavior is represented using the Lubliner damaged/plasticity model included in Abaqus [15]. This constitutive equation allows the material to behave as quasi-brittle when subjected to dominant tensile stress while it shows elastic-plastic behavior under pressure confinement and compressive loads. The tensile response is, therefore, linear and elastic with modulus and Poisson ratio, E_m and ν_m, until the tensile failure stress, σ_{t0}, is reached. Beyond this point, a quasi-brittle softening is induced in the material, with G_t being the matrix fracture energy. Under uniaxial compression, the response is linear up to the initial yield limit, σ_{c0}. Then, stress hardening takes place until the ultimate stress value is reached,

σ_{cu}. The matrix plasticity/damage model parameters used in the simulations are reported in Table 2. Fiber-matrix interface failure is taken into account using a cohesive crack approach. To this end, a cohesive interaction between the fiber and matrix surfaces is defined. The cohesive interaction is governed by a mixed-mode traction separation law where damage onset is controlled by a quadratic stress criterion with normal strength, N, and shear strength, S. Additionally, isotropic coulomb friction, ξ, after cohesive failure is included in the fiber-matrix interaction. The interface parameters used in the simulations are provided in Table 3.

E_{1f} (GPa)	E_{2f} (GPa)	ν_{12f}	ν_{23f}	G_{12f} (GPa)	G_{23f} (GPa)	α_{1f} ($10^{-6}\,°C^{-1}$)	α_{2f} ($10^{-6}\,°C^{-1}$)
231.6	12.97	0.3	0.46	11.3	4.45	-0.9	7.2

Table 1: Material properties of AS4 carbon fibers [17].

E_m (GPa)	ν_m	α_m ($10^{-6}\,°C^{-1}$)	σ_{t0} (MPa)	G_t (J/m^2)	σ_{c0} (MPa)	σ_{cu} (MPa)
231.6	0.35	52	121	90	176	180

Table 2: Parameters for the matrix damage/plasticity model [18].

N (MPa)	S (MPa)	G_N^c (J/m^2)	G_S^c (J/m^2)	ξ
57	85	7	81	0.4

Table 3: Properties of the fiber-matrix interface [18].

A previous thermal step was applied to introduce residual thermal stresses appearing due to the cooling down process after curing.

3.2 In-plane shear response

The mesoscale model utilizes a Ramberg-Osgood shear nonlinearity curve [19]. Ideally, the parameters that define the shear response are obtained from a test that isolates the behavior of a single ply subjected to large shear deformations. However, in the absence of such test data, the ASTM D3518 test of a ±45º laminate subjected to tensile loads is used to define the shear nonlinearity behavior [20]. The ±45º laminate test data smears a wide variety of damage mechanisms into a single stress-strain curve, including large fiber rotations and delamination, which are not desirable to include in the shear nonlinearity characterization. Nonetheless, given the ±45º laminate as the source of material input data for the mesoscale model, calibration of the micromechanical model was performed so that the model produced an equivalent response for an RVE in order to facilitate one-to-one comparison of the two models for the fiber kinking.

An RVE of a ±45º laminate, as shown in Figure 4b, was developed with the parameters and modeling approach described above. The dilatancy angle of the matrix, Ψ, and the temperature drop, ΔT, were adjusted to reproduce the experimental shear curves. The final response achieved from the numerical model, the experimental curve, and the Ramberg-Osgood curve fit are nearly identical as shown in Figure 4a.

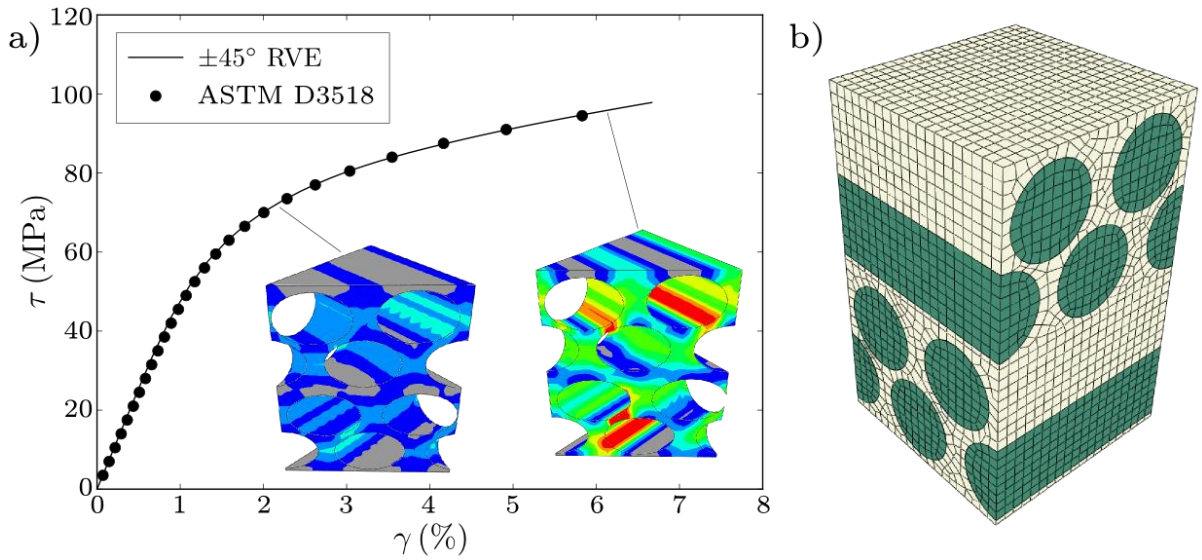

Figure 4. Shear stress-strain curves including snapshots of the plastic strain in the matrix (a) and RVE of the ±45° model (b).

4 COMPARISON OF THE MODELS

The predictions from the micromechanical model were compared with a single element analysis using the mesoscale model to understand the role of simplifying assumptions in the latter one. In both analyses, a shortening displacement in the longitudinal direction was prescribed.

The mesoscale finite element is made of one C3D8R element with a uniform edge length of 0.15 mm. The material properties used are provided in Table 4.

E_{11} (GPa)	E_{22} (GPa)	G_{12} (GPa)	ν_{12}	ν_{23}	α (MPa$^{1-\eta}$)	η	X_C (MPa)	Y_C (MPa)	S_L (MPa)
130.6	9.106	4.82	0.3	0.45	2.86 10^{-11}	6.49	1400	215	71

Table 4: AS4/8552 material properties for mesoscale model.

The results in terms of stress-strain curves up to the peak load show excellent agreement between the two models for initial misalignments ranging from 0.5 to 4° as shown in Figure 5. The CDM strength prediction follows the expression in Eq. 1, according to the nonlinear shear response described through the Ramberg-Osgood parameters (G_{12}, η, α).

The stress level (crushing stress) maintained after the peak load plotted in Figure 5a is similar in both models. The sudden load drop observed in the FEM models following the peak load is due to the dynamic nature of the numerical analyses, nevertheless the load stabilizes later and shows an asymptotic response regardless of the initial misalignment. The CDM analyses encountered some convergence difficulties and so not all cases reached the crush stress regime, especially for small initial misalignment angles.

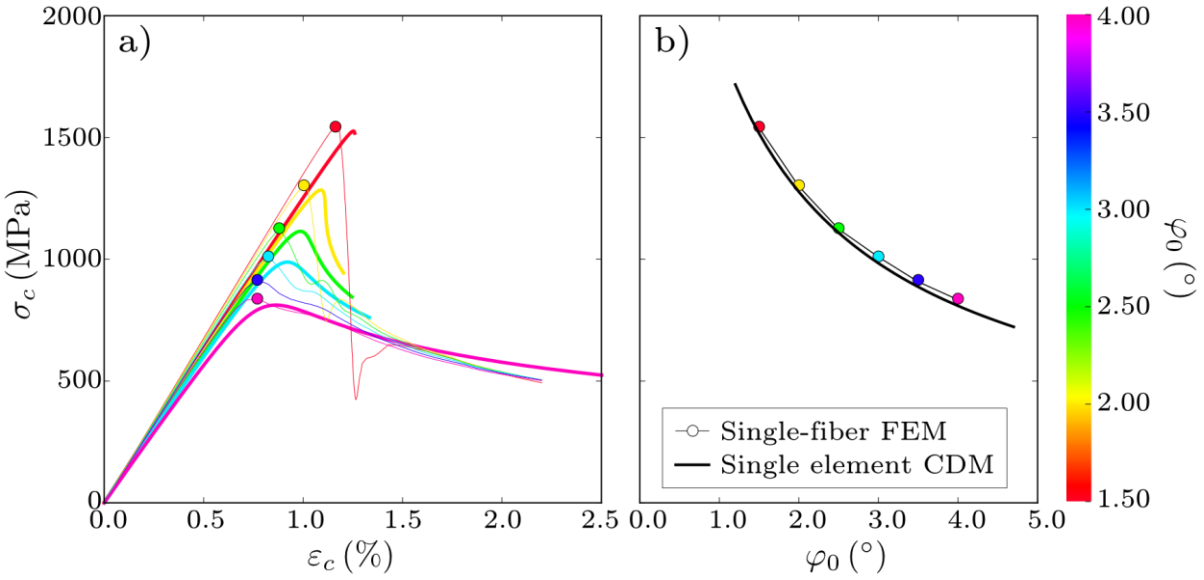

Figure 5. Comparison of the micromechanical and mesoscale CDM models under longitudinal compression for different initial misalignments: stress-strain (a) and strength-misalignment (b) curves.

Regarding the kinematics of the fiber kinking process, it is important to differentiate between the maximum, $\tilde{\varphi}$, and the average fiber rotation, $\bar{\varphi}$, see Figure 6. The maximum fiber rotation takes place in the mid-section of the fiber where $\tilde{\varphi} = \max \varphi(z)$, while the average or global rotation is based upon the deflection of the fiber as, $\bar{\varphi} = \arctan(u_y/L)$. The global rotation of the single-fiber model is comparable to the rotation of the CDM model as shown in Figure 7a, while the maximum fiber rotation is higher all along the analysis. It is observed that sudden fiber rotation occurs right after the peak load is reached, then keeps increasing linearly.

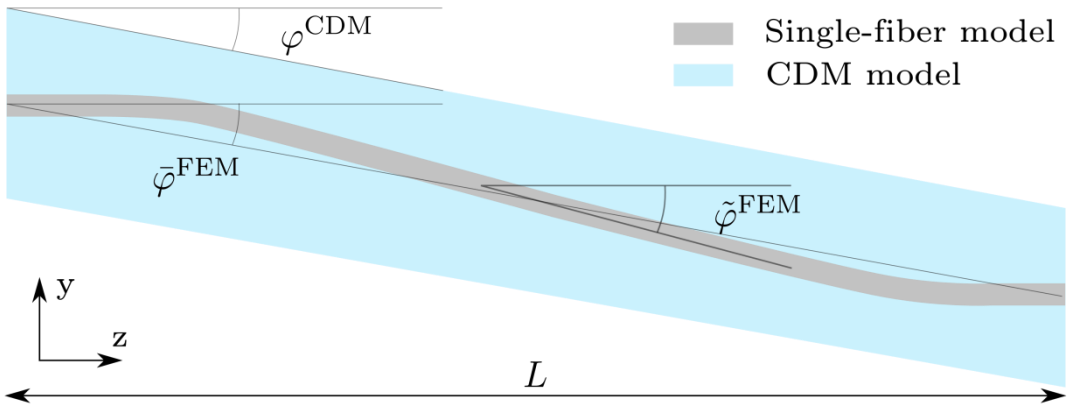

Figure 6. Interpretation of the fiber rotation kinematics due to fiber kinking

From previous experimental studies [13, 21–23], it is reported that once the kink band is generated, it propagates through the specimen at some inclination (kink angle, $10° < \beta < 30°$) with an approximately constant width. However, in the single-fiber model kink band broadening is observed due to the periodic constraints imposed in the model, as shown in Figure 7b. For this reason, kink band width increases progressively and the representative value

for w_{kb} is the one observed right after load drop, which is around $100\ \mu m \sim 15\ d_f$. The kink band width was one of the input parameters of the mesomechanical model and $w_{kb} = 100\ \mu m$ was selected for this analysis.

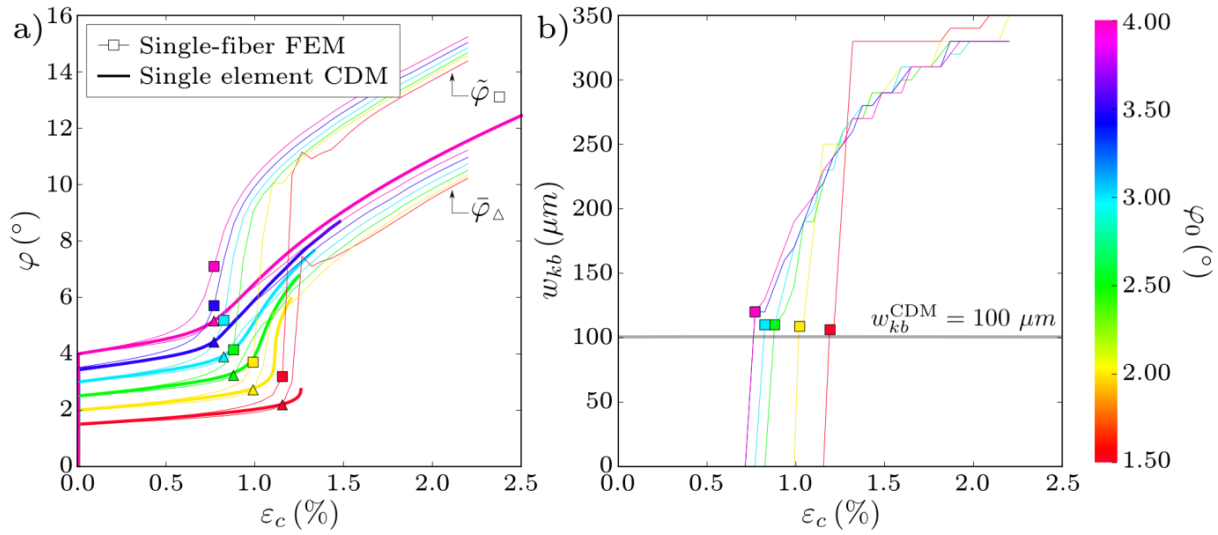

Figure 7. Comparison of the kinematics in the two models: fiber rotation (a) and kink band width (b). Markers represent the point when the peak load is reached in the FEM model: triangles stand for $\bar{\varphi}$ and squares for $\tilde{\varphi}$.

The effect of fiber-matrix friction coefficient was analyzed by conducting the same simulations with a frictionless interface ($\xi = 0$). The results of this analyses are shown in Figure 8. Although the compressive strength was barely affected, it was observed that there was a drop of approximately 30% in the crushing stress. This drop in stress is explained by the more localized kink band ($w_{kb} = 70\ \mu m - 80\ \mu m$), whose local rotation, $\tilde{\varphi}$, increases up to 30% compared to the reference case with friction. Budiansky et al. [4] related the residual crushing stress, σ_{cr}, with the in-plane shear strength of the material, S_L, and the kink band angle, β, as:

$$\sigma_{cr} = \frac{2\ S_L}{\sin 2\beta} \tag{5}$$

The single-fiber model does not represent β due to the periodic boundary conditions. Nevertheless, experimental observations from Vogler et al. [24] showed that β is proportional to the fibers rotation, φ. Thus, larger fiber rotation induces higher kink band angle sustaining lower crushing stress levels.

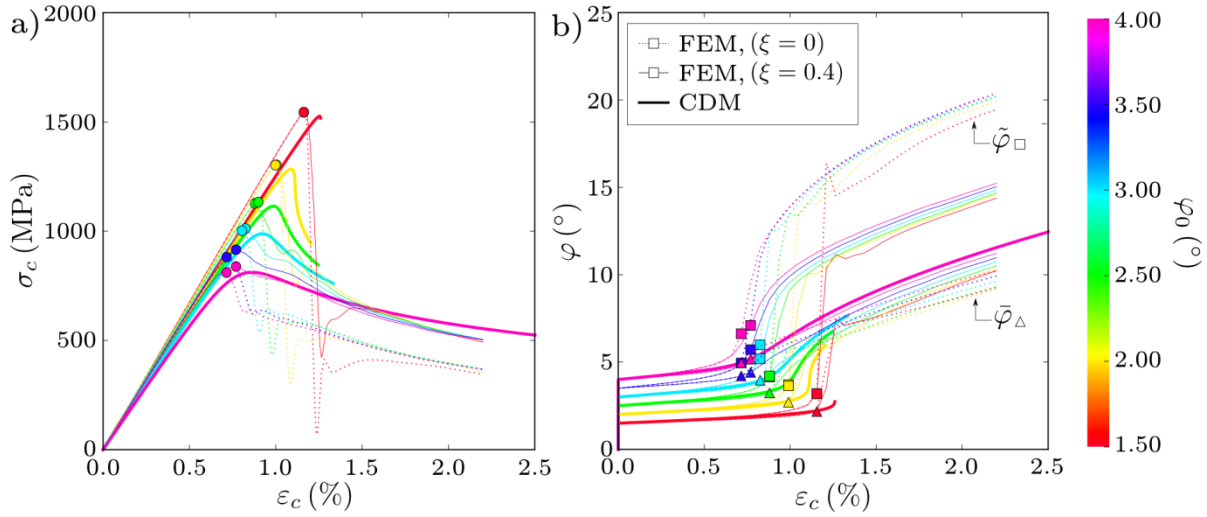

Figure 8. Results comparing the effect of the fiber-matrix friction on the fiber kinking mechanism: stress-strain curves (a) and rotation-strain curves (b) for different initial misalignments. Markers represent the point when the peak load is reached in the FEM model: triangles stand for $\bar{\varphi}$ and squares for $\tilde{\varphi}$.

5 CONCLUSIONS

In this study a computational micromechanics model is used to assess the assumptions used in the derivation of a continuum damage mechanics model considering fiber kinking failure mechanism. The continuum damage mechanics (CDM) model employs the deformation gradient decomposition (DGD) strategy and is able to capture the main features of fiber kinking such as sudden load drop, kink band formation and rotation, and holds a residual stress level (crushing).

Very good agreement was found between both models not only in terms of compressive strength prediction, but also regarding the kinematics of fiber kinking (rotation and band width) and crushing stress.

REFERENCES

[1] A. Matzenmiller, J. Lubliner, R.L. Taylor. A constitutive model for anisotropic damage in fiber-composites. *Mechanics of Materials*, **20**, 125–52, 1995. doi:10.1016/0167-6636(94)00053-0.

[2] P. Maimí, P.P. Camanho, J.A. Mayugo, C.G. Dávila. A continuum damage model for composite laminates: Part I – Constitutive model. *Mechanics of Materials*, **39**, 897–908, 2007. doi:10.1016/j.mechmat.2007.03.005.

[3] B. Budiansky, N.A. Fleck. Compressive failure of fibre composites. *Journal of the Mechanics and Physics of Solids*, **41**, 183–211, 1993. doi:10.1016/0022-5096(93)90068-Q.

[4] B. Budiansky, N.A. Fleck, J.C. Amazigo. On kink-band propagation in fiber composites. *Journal of the Mechanics and Physics of Solids*, **46**, 1637–53, 1998. doi:10.1016/S0022-5096(97)00042-2.

[5] F. Naya, M. Herráez, C.S. Lopes, C. González, S. Van der Veen, F. Pons. Computational micromechanics of fiber kinking in unidirectional FRP under different environmental conditions. *Composites Science and Technology*, **144**, 26–35, 2017. doi:10.1016/j.compscitech.2017.03.014.

[6] X. Bai, M.A. Bessa, A.R. Melro, P.P. Camanho, L. Guo, W.K. Liu. High-fidelity micro-scale modeling of the thermo-visco-plastic behavior of carbon fiber polymer matrix composites. Composite Structures, **134**, 132–41, 2015. doi:10.1016/j.compstruct.2015.08.047.

[7] A.C. Bergan, F.A. Leone. A continuum Damage Mechanics Model to Predict Kink-Band Propagation Using Deformation Gradient Tensor Decomposition. Presented at the American Society for Composites 31st Technical Conference, 2016.

[8] F.A. Leone. Deformation gradient tensor decomposition for representing matrix cracks in fiber-reinforced materials. *Composites Part A Applied Science and Manufacturing*, **76**, 334–41, 2015. doi:10.1016/j.compositesa.2015.06.014.

[9] Z.P. Bazant, B.H. Oh. Crack Band Theory for Fracture of Concrete. *Matériaux et Construction*, **16**, 155–77, 1983.

[10] S. Costa, R. Gutkin, R. Olsson. Mesh objective implementation of a fibre kinking model for damage growth with friction. Composite Structures, **168**, 384–91, 2017. doi:10.1016/j.compstruct.2017.02.057.

[11] M.J. Laffan, S.T. Pinho, P. Robinson, L. Iannucci, A.J. McMillan. Measurement of the fracture toughness associated with the longitudinal fibre compressive failure mode of laminated composites. *Composites Part A Applied Science and Manufacturing*, **43**, 1930–8, 2012. doi:10.1016/j.compositesa.2012.04.009.

[12] D. Svensson, K.S. Alfredsson, U. Stigh, N.E. Jansson. Measurement of cohesive law for kink-band formation in unidirectional composite. *Engineering Fracture Mechanics*, **151**, 1–10, 2016. doi:10.1016/j.engfracmech.2015.10.040.

[13] S. Pimenta, R. Gutkin, S.T. Pinho, P. Robinson. A micromechanical model for kink-band formation: Part I — Experimental study and numerical modelling. *Composite Science and Technology*, **69**, 948–55, 2009. doi:10.1016/j.compscitech.2009.02.010.

[14] S.T. Pinho, P. Robinson, L. Iannucci. Fracture toughness of the tensile and compressive fibre failure modes in laminated composites. *Composite Science and Technology*, **66**, 2069–79, 2006. doi:10.1016/j.compscitech.2005.12.023.

[15] Simulia, editor. Abaqus Analysis User's Guide. Version 6.13. 2013.

[16] R. Gutkin, S.T. Pinho, P. Robinson, P.T. Curtis. On the transition from shear-driven fibre compressive failure to fibre kinking in notched CFRP laminates under longitudinal compression. *Composite Science and Technology*, **70**, 1223–31, 2010. doi:10.1016/j.compscitech.2010.03.010.

[17] M. Herráez, D. Mora, F. Naya, C.S. Lopes, C. González, J. Llorca. Transverse cracking of cross-ply laminates: A computational micromechanics perspective. *Composite Science and Technology*, **110**, 196–204, 2015. doi:10.1016/j.compscitech.2015.02.008.

[18] L.P. Canal, J. LLorca, C. González, J. Segurado. Intraply fracture of fiber-reinforced composites: Microscopic mechanisms and modeling. *Composite Science and Technology*, **72**, 1223–32, 2012.

[19] W. Ramberg, W.R. Osgood. Description of Stress-Strain Curves by Three Parameters. NACA Technical Note No. 902, 1943.

[20] ASTM Standard D3518. Standard Test Method fon In-Plane Shear Response of Polymer Matrix Composite Materials by Tensile Test of a ±45° Laminate. Annual

Book of ASTM Standards, ASTM International, 2013.

[21] M.R. Piggott, B. Harris. Factors affecting the compression strength of aligned fibre composites. *Advanced Composite Materials*, 305–12, 1980. doi:10.1016/B978-1-4832-8370-8.50027-9.

[22] S. Kyriakides, R. Arseculeratne, E.J. Perry, K.M. Liechti. On the compressive failure of fiber reinforced composites. *International Journal of Solids and Structures*, **32**, 689–738, 1995. doi:10.1016/0020-7683(94)00157-R.

[23] C.R. Schultheisz, A.M. Waas. Compressive failure of composites, Part I: Testing and micromechanical theories. *Progress in Aerospace Sciences*, **32**, 1–42, 1996. doi:10.1016/0376-0421(94)00002-3.

[24] T.J. Vogler, S. Kyriakides. Initiation and axial propagation of kink bands in fiber composites. *Acta Materialia*, **45**, 2443–54, 1997. doi:10.1016/S1359-6454(96)00350-3.